

This is an Open Access document downloaded from ORCA, Cardiff University's institutional repository: <https://orca.cardiff.ac.uk/id/eprint/110604/>

This is the author's version of a work that was submitted to / accepted for publication.

Citation for final published version:

Lee, Sung Su, Kim, Young-Min, Lee, Hyun-Jae, Seo, Okkyun, Jeong, Hu Young, He, Qian, Borisevich, Albina Y., Kang, Boyoun, Kwon, Owoong, Kang, Seunghun, Kim, Yunseok, Koo, Tae Yeong, Rhyee, Jong-Soo, Noh, Do Young, Cho, Beongki, Seo, Ji Hui, Lee, Jun Hee and Jo, Ji Young 2018. Correlation between Geometrically induced oxygen octahedral tilts and multiferroic behaviors in BiFeO<sub>3</sub> films. *Advanced Functional Materials* 28 (19), 1800839. 10.1002/adfm.201800839

Publishers page: <http://dx.doi.org/10.1002/adfm.201800839>

Please note:

Changes made as a result of publishing processes such as copy-editing, formatting and page numbers may not be reflected in this version. For the definitive version of this publication, please refer to the published source. You are advised to consult the publisher's version if you wish to cite this paper.

This version is being made available in accordance with publisher policies. See <http://orca.cf.ac.uk/policies.html> for usage policies. Copyright and moral rights for publications made available in ORCA are retained by the copyright holders.



# Correlation between Geometrically Induced Oxygen Octahedral Tilts and Multiferroic Behaviors in BiFeO<sub>3</sub> Films

Sung Su Lee, Young-Min Kim, Hyun-Jae Lee, Okkyun Seo, Hu Young Jeong, Qian He, Albina Y. Borisevich, Boyoun Kang, Owoong Kwon, Seunghun Kang, Yunseok Kim, Tae Yeong Koo, Jong-Soo Rhyee, Do Young Noh, Beongki Cho, Ji Hui Seo, Jun Hee Lee, and Ji Young Jo\*

The equilibrium position of atoms in a unit cell is directly connected to crystal functionalities, e.g., ferroelectricity, ferromagnetism, and piezoelectricity. The artificial tuning of the energy landscape can involve repositioning atoms as well as manipulating the functionalities of perovskites (ABO<sub>3</sub>), which are good model systems to test this legacy. Mechanical energy from external sources accommodating various clamping substrates is utilized to perturb the energy state of perovskite materials fabricated on the substrates and consequently change their functionalities; however, this approach yields undesired complex behaviors of perovskite crystals, such as lattice distortion, displacement of B atoms, and/or tilting of oxygen octahedra. Owing to complimentary collaborations between experimental and theoretical studies, the effects of both lattice distortion and displacement of B atoms are well understood so far, which leaves us a simple question: Can we exclusively control the positions of oxygen atoms in perovskites for functionality manipulation? Here the artificial manipulation of oxygen octahedral tilt angles within multiferroic BiFeO<sub>3</sub> thin films using strong oxygen octahedral coupling with bottom SrRuO<sub>3</sub> layers is reported, which opens up new possibilities of oxygen octahedral engineering.

## 1. Introduction

In ABO<sub>3</sub> perovskite oxides, consisting of an oxygen octahedron and two kinds of positive ions (A and B), the oxygen octahedral tilt (OOT) of the crystal is linked to electrical<sup>[1,2]</sup> and/or magnetic<sup>[3,4]</sup> behaviors, since the tilt angle associates with both the length and angle of the B O B bond via overlap of the *d* orbitals and localized charge carriers.<sup>[5]</sup> Control of the OOT angle can allow us to engineer electrical and magnetic behaviors and to examine the complex relationships between the oxygen octahedral structure and multifunctionalities of perovskite oxides.<sup>[6–9]</sup> As well as engineering of cation chemistry in bulk powder forms, the application of an in-plane biaxial strain arising from lattice mismatch between a substrate and a film (via varying film thickness or substrate substance) has been typically employed

S. S. Lee, Dr. O. Seo, Dr. B. Kang, Prof. B. Cho, Prof. J. Y. Jo  
School of Materials Science and Engineering  
Gwangju Institute of Science and Technology  
Gwangju 61005, South Korea

E-mail: jyjo@gist.ac.kr

Prof. Y.-M. Kim  
Department of Energy Science  
Sungkyunkwan University (SKKU)  
Suwon 16419, South Korea

Prof. Y.-M. Kim  
Center for Integrated Nanostructure Physics  
Institute for Basic Science (IBS)  
Suwon 16419, South Korea

H.-J. Lee, J. H. Seo, Prof. J. H. Lee  
School of Energy and Chemical Engineering  
Ulsan National Institute of Science and Technology  
Ulsan 44919, South Korea

Prof. H. Y. Jeong  
UNIST Central Research Facilities (UCRF)  
Ulsan National Institute of Science and Technology  
Ulsan 44919, South Korea

Dr. Q. He, Dr. A. Y. Borisevich  
Materials Science and Technology Division  
Oak Ridge National Laboratory  
Oak Ridge, TN 37831, USA

Dr. Q. He  
Cardiff Catalyst Institute  
School of Chemistry  
Cardiff University  
Cardiff CF10 3AT, UK

O. Kwon, S. Kang, Prof. Y. Kim  
School of Advanced Materials Science and Engineering  
Sungkyunkwan University (SKKU)  
Suwon 16419, South Korea

Dr. T. Y. Koo  
Pohang Accelerator Laboratory  
Pohang 37673, South Korea

Prof. J.-S. Rhyee  
Department of Applied Physics and Institute of Natural Sciences  
Kyung Hee University  
Yongin 17104, South Korea

Prof. D. Y. Noh  
Department of Physics and Photon Science  
Gwangju Institute of Science and Technology  
Gwangju 61005, South Korea

 The ORCID identification number(s) for the author(s) of this article can be found under <https://doi.org/10.1002/adfm.201800839>.

to distort the lattice structure, tilt the oxygen octahedra.<sup>[10–13]</sup> However, in-plane biaxial-strain variations change the electrostatic boundary conditions as well as OOT behavior, along with degradation of crystallinity.<sup>[14]</sup> So, the bona fide control of the OOT angle, without changing the in-plane biaxial strain state and boundary conditions, has not thus far been realized, which hinders us from understanding the direct connection between the OOT behavior and perovskite oxide functionalities.

BiFeO<sub>3</sub> (BFO), which exhibits both ferroelectricity and anti-ferromagnetism at room temperature, is a suitable model system to investigate the effects of the OOT on its emerging functionalities.<sup>[15–17]</sup> In bulk, rhombohedral BFO possesses an isotropic Fe–O–Fe bond angle and isotropic tilt angle of 13.8° around the pseudocubic axes along with shift of Fe<sup>3+</sup> ions from the center of the oxygen octahedra by 0.134 Å along the three-fold axis.<sup>[18]</sup> In thin film form, depending on the magnitude of the in-plane biaxial strain, BFO with other crystallographic phases (such as tetragonal or monoclinic phase) can possess anisotropic tilt angles along with Fe–O–Fe bond-angle variation.<sup>[1,19]</sup> The in-plane biaxial strain can change the magnitude of cation displacement linked to ferroelectricity<sup>[1,19,20]</sup> and induce nonperfect antiparallel arrangement of Fe<sup>3+</sup> ions linked to weak ferromagnetism.<sup>[21–23]</sup> However, there has been no consensus on a quantitative relationship between the in-plane biaxial strain, octahedral tilt angle, atomic displacement, and net magnetization in particular.<sup>[24–27]</sup>

The OOT pattern of the bottom layer can be used to quantitatively control that of the upper layer film via an interfacial corner-shared connection. Here we report room temperature multiferroicity of BFO thin film can be dramatically manipulated through the control of OOT behavior without any variation of in-plane biaxial strain, which is achieved via atomic-scale growth template design. Both the crystallographic structure and OOT angles of the bottom platform layer fully influence into the upper BFO films without any in-plane-biaxial-strain variation via the artificial design of platform layer. We further clarify the correlation between the OOT angle, atomic displacement, ferroelectricity, and net magnetization of BFO films. The OOT angle control via oxygen-position manipulation provides a pragmatic platform to manipulate lattice-coupled ferroic order parameters including the enhancement of ferroelectricity and the realization of unprecedented magnetization.

## 2. Crystalline Structure of BiFeO<sub>3</sub>/SrRuO<sub>3</sub> Films Grown on SrTiO<sub>3</sub> Substrate

After preparing monoclinic-SrRuO<sub>3</sub> (M-SRO) and tetragonal-SrRuO<sub>3</sub> (T-SRO) films on (001)-oriented SrTiO<sub>3</sub> (STO) substrates via oxygen-partial-pressure control during the growth process (M and T stand for monoclinic and tetragonal, respectively), BFO films were epitaxially grown on these two types of SRO films; the corresponding X-ray diffraction (XRD) patterns are shown in **Figure 1a**. The Laue oscillations across the BFO (2) and SRO (002) reflections along the *L*-direction (inset of Figure 1a) indicate the smooth surfaces of both the BFO and SRO films. The observed similar widths of reflection peaks for BFO films, SRO films, and STO substrates along the *H*-direction (Figure S1a,b, Supporting Information) indicate that the

crystalline qualities of the films are identical with that of the single-crystalline STO substrate. The observed vertical alignment of all the BFO, SRO, and STO (103) reflections indicates that all the BFO and SRO films are completely strained with respect to the STO substrates, as shown in Figure S1a,b in the Supporting Information. Regardless of the structural phase, all the BFO and SRO films possess the same in-plane lattice parameter of 3.905 Å, whose value is even smaller than those of the BFO and the SRO bulk materials corresponding to 3.965 and 3.928 Å, respectively. The in-plane constraint for BFO and SRO films results in an elongation of the out-of-plane lattice parameter, as tabulated in Table S1 in the Supporting Information.

Despite the identical in-plane lattice constant, the crystallographic structure of the BFO films depends on that of corresponding bottom SRO film; e.g., the M-BFO film was grown on the M-SRO film and the T-BFO film was grown on the T-SRO film. In the *L*-scans of the BFO film on M-SRO film (Figure S1c, Supporting Information), the (102), (012), and (−1 02) reflection peaks for both BFO and M-SRO films are split along the *L*-direction, which indicates that the crystallographic structure of BFO on M-SRO film is also the M phase structure.<sup>[28]</sup> As shown in Figure S1d in the Supporting Information, in contrast, the (102), (012), and (−1 02) reflection peaks of BFO film on T-SRO film are not split, thereby indicating that the crystallographic structure of BFO on T-SRO film is the T phase structure. Based on the distance between the (102) and (−1 02) reflection peaks along the *L*-direction, as shown in Figure S1c,d in the Supporting Information, the monoclinic distortion angles of M-BFO and M-SRO films were estimated as 0.19° and 0.12°, respectively. Our results indicate that the crystal structure of the bottom SRO layer plays a critical role in determining the crystal structure of the epitaxial BFO films.

## 3. Control of Octahedral Structure and Fe-Ion Displacement in BiFeO<sub>3</sub>/SrRuO<sub>3</sub> Films

The oxygen octahedral structure of all the BFO and SRO films was investigated by monitoring the intensities of the half-integer reflections. Figure 1b shows the schematic of the tilt axes and angles of the oxygen octahedra. When the in-phase OOT along the pseudocubic [100], [010], or [001] directions, 1/2 (even, odd), 1/2 (odd, even, odd), or 1/2 (odd, odd, even) reflections are allowed to appear.<sup>[29]</sup> When the oxygen octahedra and the nearest-neighbor oxygen octahedra tilt in opposite directions along the pseudocubic [100], [010], or [001] directions, only 1/2 (odd, odd, odd) reflections are allowed to appear. The allowed half-integer reflections for all types of OOT are summarized in Table S2 in the Supporting Information. In this regard, Glazer reported the classification of the OOT in perovskite oxides using symbols, where *a*, *b*, and *c* represent the octahedral tilt angles along the [100], [010], and [001] directions, respectively, and the superscripts of +, −, and 0 refer to in-phase, antiphase, and no-tilt conditions between the nearest neighboring octahedra<sup>[29,30]</sup>. For example,  $a^-b^-c^-$  represents a unit cell with three unequal tilt angles and  $a^-a^-a^-$  represents a unit cell with equal tilt angles.

A high-flux synchrotron X-ray source was used to identify these half-integer reflections of the BFO/SRO films because

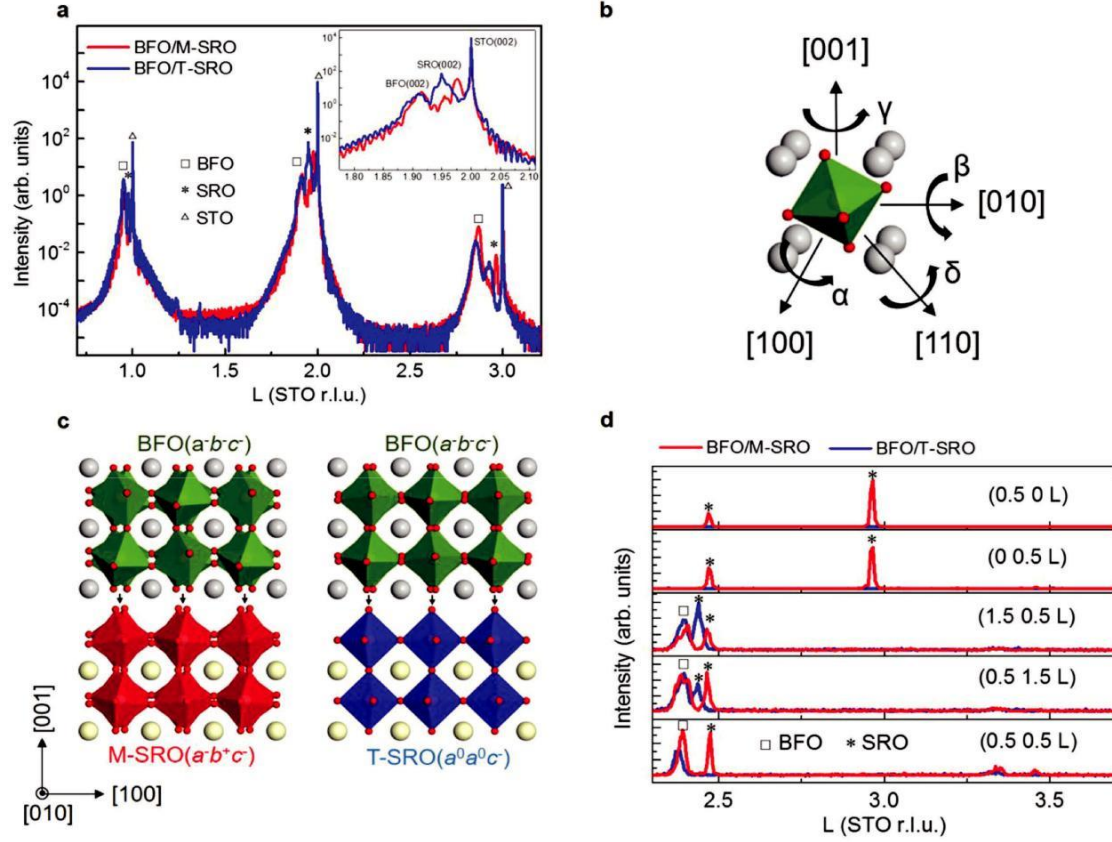


**Figure 1.** Crystal structure and oxygen octahedral pattern of BFO/M-SRO and BFO/T-SRO films. a) Reciprocal space (00L) scans of M-BFO/M-SRO/STO(001) (red) and T-BFO/T-SRO/STO(001) films (blue). b) Schematic of tilt axes and angles of oxygen octahedra. c) Schematic models of oxygen octahedral patterns for BFO/M-SRO and BFO/T-SRO. We defined the out-of-plane direction as  $[001]_{pc}$  axes, which is the direction of film growth. d) (from top to bottom) Reciprocal space L-scans around half-integer reflections along  $(0.5\ 0\ L)$ ,  $(0\ 0.5\ L)$ ,  $(1.5\ 0.5\ L)$ ,  $(0.5\ 1.5\ L)$ , and  $(0.5\ 0.5\ L)$ . and \* marks indicate the diffraction peaks originated from BFO and SRO films.

the intensity of half-integer reflections is weaker by a factor of 4 than that of Bragg reflections due to the small atomic form factor of oxygen ions. The oxygen octahedral structure of M-SRO, T-SRO, M-BFO, and T-BFO films are  $a^-b^+c^-$ ,  $a^0b^-c^-$ ,  $a^-b^-c^-$ , and  $a^-b^-c^-$ , respectively, as displayed in Figure 1c. Figure 1d shows the L-scans of all the BFO and SRO films with T or M phases. Based on a set of L-scans, the octahedral tilt types for both BFO and SRO films with T or M phases can be determined as follows: In the M-SRO film,  $b^+$  tilting generates the  $(0.5\ 0\ 2.5)$  and  $(0\ 0.5\ 2.5)$  peaks, while  $c^-$  tilting generates the  $(1.5\ 0.5\ 2.5)$  and  $(0.5\ 1.5\ 2.5)$  peaks. In addition,  $a^-$  tilting generates  $(0.5\ 0.5\ 2.5)$  and  $(0.5\ 0.5\ 3.5)$  reflections. In the T-SRO film, there are no signs of  $(0.5\ 0\ 2.5)$ ,  $(0\ 0.5\ 2.5)$ , and  $(0.5\ 0.5\ 2.5)$  reflections, which implies  $a^0$  tilting. In both BFO films, the absence of  $(0.5\ 0\ 2.5)$ ,  $(0\ 0.5\ 2.5)$ ,  $(0.5\ 1.5\ 3)$ , and  $(1.5\ 0.5\ 3)$  reflections along with the existence of  $(0.5\ 1.5\ 2.5)$ ,  $(1.5\ 0.5\ 2.5)$ , and  $(0.5\ 0.5\ 2.5)$  reflections suggested  $a^-b^-c^-$  tilting. The intensity of the  $(0.5\ 0.5\ 2.5)$  reflection for the M-BFO film is twice that of the T-BFO film, as shown in Figure 1d, implying that the  $\delta$  value of M-BFO is also larger than that of the T-BFO.<sup>[11,12]</sup> However, based on the XRD results for half-integer reflections, the magnitude of  $\delta$  cannot be completely determined for all the films.

The different OOT behaviors of the two M-BFO/M-SRO and T-BFO/T-SRO films were directly visualized at the atomic scale

via annular bright field (ABF)-scanning transmission electron microscopy (STEM), which can detect both light and heavy elements and show the atomic columns as dark features in the images.<sup>[31]</sup> A well-developed computational tracking method of the oxygen positions and B O B angles in the ABF-STEM image can allow mapping of the actual spatial  $BO_6$  tilt patterns in complex oxides  $ABO_3$  with unit-cell resolution.<sup>[32]</sup> The ABF-STEM images and the corresponding octahedral tilt maps obtained via the atom position quantification process are depicted in the upper panels of Figure 2a,b. Each pixel in the maps represents a sublattice consisting of four Bi atoms, and the intensity of the pixel indicates the value of the OOT angle at the sublattice.<sup>[33]</sup> The tilt angles in the BFO film viewed along the  $[110]$  pseudocubic orientation are geometrically measured to be oscillating along the in-plane direction. Thus, this antiphase character of the in-plane tilt can be generated as a checker-board contrast in the map, similar to previous studies.<sup>[1,19,33]</sup> The graphs at the bottom of each map in Figure 2 show the line profiles averaged over the vertical rows of the respective maps. Due to strong interface coupling of the octahedral corner connectivity between BFO/SRO, a gradual transition of the tilt occurs across the interface within 4–5 unit cells. Clear differences between the tilt behaviors are observed for the two BFO films; a distinctive reduction in the octahedral tilt with a

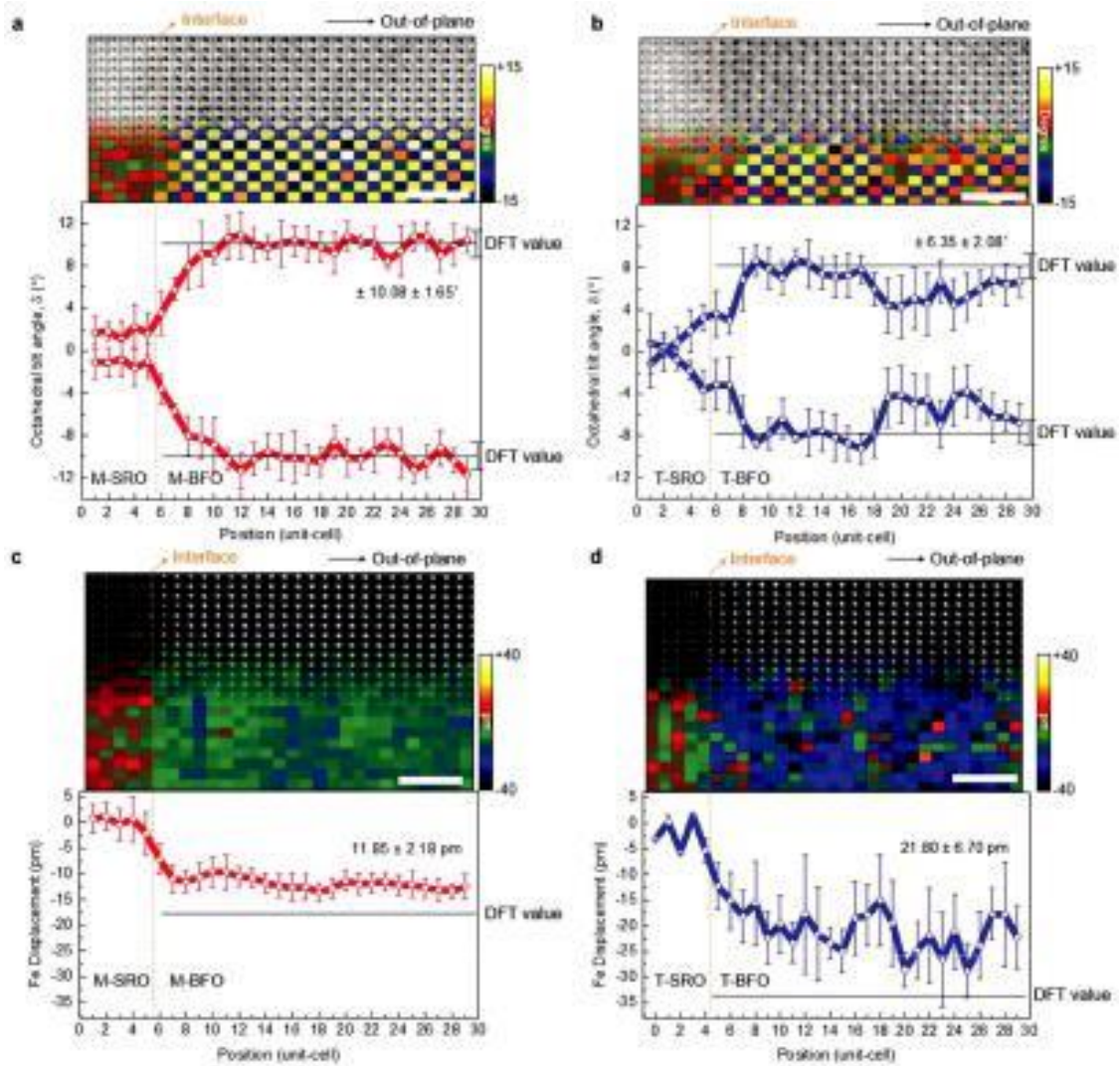


**Figure 2.** Atomic position mapping of M-BFO/M-SRO and T-BFO/T-SRO films. a,b) Pairwise representations of annular bright field scanning transmission electron microscopy (ABF-STEM) images showing oxygen column contrast and the resulting octahedral tilt maps showing checkerboard pattern of the tilt (top panels) for both pseudocubic [110]<sub>pc</sub>-oriented BFO thin films, (a) M-BFO and (b) T-BFO, grown on different SRO films. The bottom panels in each figure show the corresponding line profiles averaged over vertical rows of the respective tilt maps. Blue lines in each graph indicate calculated tilt angles in the BFO structure by DFT methods. c,d) Pairwise representations of high-angle annular dark field scanning transmission electron microscopy (HAADF-STEM) images and out-of-plane Fe displacement maps (top panels in each figure) and the corresponding averaged line profiles (bottom panels) for both BFO films that are aligned along the pseudocubic [110]<sub>pc</sub> orientation. Blue lines in each graph indicate displacement of Fe in BFO calculated by DFT methods. Orange dotted lines in each graph represent interfaces between each SRO and BFO structure. A single rectangular pixel in the map corresponds to a sublattice consisting of four Bi atoms as a basis. The scale bar is 2 nm.

$\delta$  value of  $6.35^\circ \pm 2.08^\circ$  is observed for T-BFO as compared with M-BFO showing a  $\delta$  value of  $10.08^\circ \pm 1.65^\circ$  that is similar to the value expected in typical bulk monoclinic BFO ( $H10.5^\circ$  for this projection).<sup>[19]</sup> It is noteworthy that the tilt values obtained from the ABF-STEM image simulations performed with the two models derived by density functional theory (DFT) calculations show excellent agreement with the experimentally measured values; the corresponding DFT values are marked in each graph, and the tilt mapping results for the two models are provided in Figure S2 in the Supporting Information. These real-space measurements of the tilts for the two BFO films directly corroborate the aforementioned reciprocal space X-ray analysis. Here, we remark that the different tilt behaviors of the M-SRO

and T-SRO films were mapped out for the [100] pseudocubic orientation as the projected tilt angles can be imaged along that direction (see Figure S3 in the Supporting Information); a significant octahedral tilt was only observed for M-SRO, which is consistent with the results of X-ray analysis.

The polarization behaviors of the two BFO films were characterized by mapping the relative Fe cation displacements. To this end, we used high-angle annular dark field (HAADF)-STEM to determine the 2D atom positions numerically with picometer-scale precision.<sup>[34]</sup> In the HAADF-STEM imaging mode, the contrast of the atomic column appears bright and is roughly scaled to the square of the atomic number.<sup>[35]</sup> Figure 2c,d shows the maps and corresponding profiles of the

out-of-plane off-center displacements of the Fe cations relative to the Bi sublattice; the off-center displacements are observed to increase as the magnitude of BFO polarization increases.<sup>[36–38]</sup> Fe cations for both films are shown to be displaced along the out-of-plane growth direction (hence the negative values in the profiles), thus indicating polarizations of both films by actual observation point toward the interface. In marked contrast, the T-BFO film with the lower tilt angle exhibits a larger magnitude ( $21.80 \pm 6.70$  pm) of Fe cation displacement than that ( $11.85 \pm 2.18$  pm) of the M-BFO, which exhibits a value similar to that of bulk BFO (13.4 pm).<sup>[18]</sup>

#### 4. Weak-Ferromagnetic and Ferroelectric Behaviors in BiFeO<sub>3</sub>/SrRuO<sub>3</sub> Films

To investigate the effects of OOT on the magnetic order parameters, the magnetization of M-BFO/M-SRO and T-BFO/T-SRO films was acquired via magnetization–magnetic-field hysteresis curves, as shown in **Figure 3**. At room temperature, all the BFO films exhibit a weak ferromagnetic behavior under the application of a magnetic field parallel to the [001]<sub>pc</sub> and [100]<sub>pc</sub> directions. The STO substrate and SRO layer, which are room-temperature diamagnetic and paramagnetic,<sup>[39]</sup> respectively, can contribute a linear magnetic-field-dependent magnetization to the magnetization–magnetic-field hysteresis curves. The magnetization of the BFO films was acquired by subtracting the diamagnetic and paramagnetic signals arising from the STO substrate and SRO films (see Figure S4 in the Supporting Information), respectively. The out-of-plane net magnetizations of M-BFO/M-SRO and T-BFO/T-SRO films are 0.019 and 0.009  $\mu_B/\text{Fe}$ , respectively. The observed increment in the net magnetization of M-BFO/M-SRO film by a factor of 2 implies that the  $\delta$  value of the M-BFO/M-SRO film is larger than the T-BFO/T-SRO film.<sup>[21]</sup>

Please note that the in-plane net magnetizations of M-BFO/M-SRO and T-BFO/T-SRO films are 0.047 and 0.010  $\mu_B/\text{Fe}$ , respectively, whose values of M-BFO agree with the results for BFO/SRO(50 nm)/STO films.<sup>[26]</sup> Here, we remark that there has been uncertainty on the correlation between the

net magnetization and in-plane biaxial strain on BFO film<sup>[24–27]</sup>, however, our results show that the tilt angles can change the net magnetization of BFO films regardless of the film thickness and in-plane biaxial strain. We believe that our results can shed light on the direct correlation between the net magnetization and OOT angles. For both BFO/SRO films, the net magnetization along the in-plane direction is larger than that along the out-of-plane direction. For M-BFO/M-SRO and T-BFO/T-SRO films, the net magnetizations along the in-plane direction are 2.4 and 1.1 times larger than the corresponding ones of the out-of-plane direction, respectively.

The polarization behavior should correlatively differ in the two BFO films due to the strong connection between the structure and charge degrees of freedom.<sup>[25]</sup> In order to investigate the ferroelectric characteristics of BFO with different off-center displacements, domain writing, and hysteresis loop measurements were performed along the out-of-plane direction at room temperature. In the piezoresponse force microscopy (PFM) amplitude and phase images in **Figure 4a–d**, the outermost box patterns indicate that M-BFO/M-SRO and T-BFO/T-SRO films possess downward monodomains in the as-grown condition while the innermost box patterns indicate a switched region via a writing process with the application of voltages as high as +6 V (see Note 2 in the Supporting Information for lateral PFM images). As shown in Figure 4e, the hysteresis loops of both M-BFO/M-SRO and T-BFO/T-SRO films exhibit a ferroelectric switching behavior with coercive voltages of +2 V and –3 V, respectively. It is notable that the positive remnant piezoresponse of the T-BFO/T-SRO film is larger than that of the M-BFO/M-SRO film by a factor of 1.6.

To check if there is a probability of chemical perturbation effects (due to cation off-stoichiometry and/or oxygen vacancies) on the manifested multiferroic behaviors of the two BFO films, we performed XPS and atomic-scale STEM-energy dispersive X-ray spectrometer (EDS)/electron energy loss spectrometer (EELS) experiments. As a result, it is clarified that the two BFO films are chemically identical to each other with the full oxygen stoichiometry (see Note 1 in the Supporting Information).

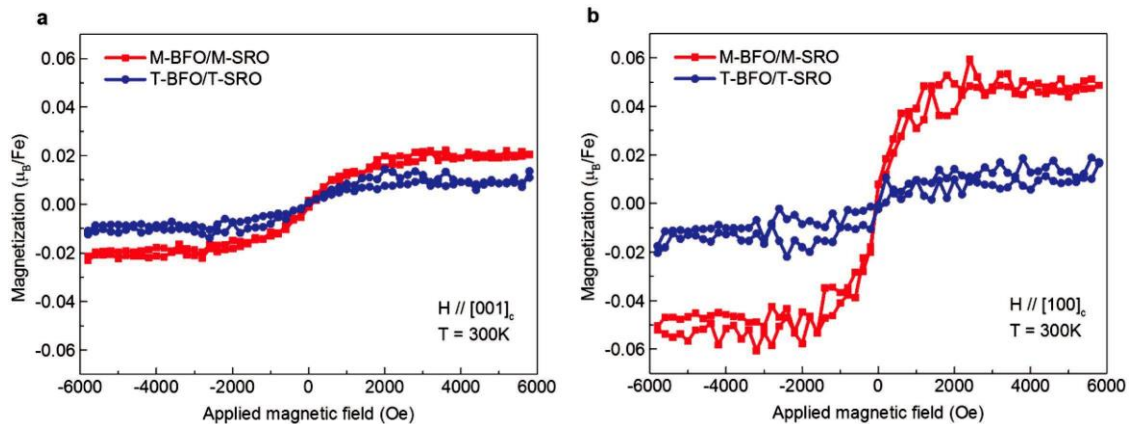


**Figure 3.** Magnetic hysteresis loops of M-BFO/M-SRO and T-BFO/T-SRO films. a,b) Hysteresis curves at 300 K after subtraction of both the paramagnetic and diamagnetic background signals arising from the SRO film and the STO substrate, respectively. Before magnetic measurements, the rear and side surface of the substrates was polished in order to eliminate noise from impurities. (a) Magnetometer axis is out-of-plane, which is parallel to the [001]<sub>pc</sub> direction of STO substrates. (b) Magnetometer axis is in-plane, which is parallel to the [100]<sub>pc</sub> direction of STO substrates.

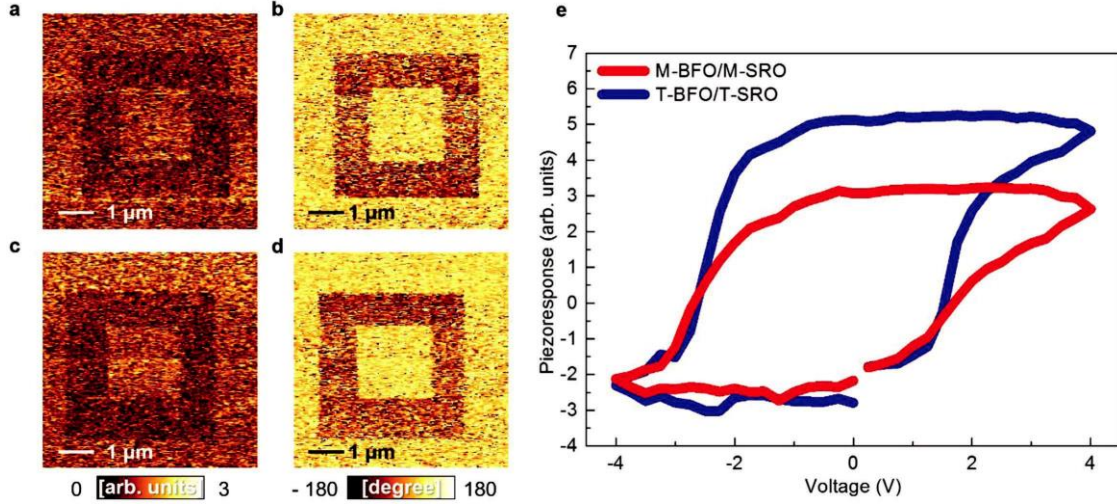


**Figure 4.** Piezoresponse force microscopy (PFM) images of M-BFO/M-SRO and T-BFO/T-SRO films after electrical poling. a–d) Ferroelectric domain patterns after application of  $-6$  V over area of  $4 \times 4 \mu\text{m}^2$  and subsequently  $+6$  V over  $2 \times 2 \mu\text{m}^2$  inside: PFM amplitude image for (a), M-BFO/M-SRO and (c), T-BFO/T-SRO films. PFM phase images for (b), M-BFO/M-SRO and (d), T-BFO/T-SRO films. e) Piezoresponse–voltage hysteresis loops for M-BFO/M-SRO and T-BFO/T-SRO films.

## 5. DFT Calculation Results of BiFeO<sub>3</sub>/SrRuO<sub>3</sub> Films

A DFT was employed to demonstrate the physical correlation between the OOT angles and subsequent ion displacements of M-BFO/M-SRO and T-BFO/T-SRO films. Under a fixed in-plane lattice constant of SrTiO<sub>3</sub>, by relaxing two different geometries close to those of the M-BFO and T-BFO observed experimentally, we derived two isosymmetric structural phases from the DFT calculations; notably, the one close to M-BFO was found to have the monoclinic space group (*Cc*) and the other close to T-BFO was proved to be similar to *Ima2* structure with  $\gamma$  being reduced. The  $\delta$  angles and the magnitude of Fe off-centering for the former and latter structures were measured to be  $10^\circ$ ,  $8^\circ$ ,  $18$  pm, and  $34$  pm, respectively, thus indicating that the optimized structure close to the experimental T-BFO has a larger magnitude of Fe off-centering and a lower tilt value as compared to the structure close to the experimental M-BFO. This result is remarkably consistent with the experimental observations performed by our quantitative STEM approach. We note that the magnitudes of Fe off-centering in the two models show a little bit larger values than those of the experimental measurements, while the calculated tilt angles are excellently corresponding to those measured in experiments. This discrepancy might be attributed to the thin film effect.<sup>[40]</sup> Given the experimental results combined with the DFT calculations, we clearly see that the interplay between local cation displacements and octahedral tilt changes strongly affects the ferroic order parameters of the BFO films. A further notable discovery is that the intriguing coupling behavior of the structural order parameters appears to be sustained up to at least  $H_{25}$  nm away from the interface region (see Figures S5 and S6 in the Supporting Information), which means that the polarization and magnetic behaviors associated with the induced structural transitions of BFO films by the strong interfacial tilt coupling can change in a long range that might reach over the whole area.

In regard to the ferroic order parameters of BiFeO<sub>3</sub> films, our findings allow us to draw two important consequences: First, the net magnetization arising from antisymmetric spin coupling can be tuned by changing the OOT angle.<sup>[21]</sup> Second, the ferroelectric polarization that is manifested from the relative Fe-ion displacement can be engineered by the control of OOT. From the DFT calculations that can provide a theoretical estimation of the polarization and the net magnetization for the two phases, it is revealed that the reduction in tilt angle from M-BFO to T-BFO (as shown in Figure 2) can cause a significant increase in the ferroelectric polarization from  $47$  to  $80 \mu\text{C cm}^{-2}$ . From M- to T-BFO, the DFT calculations predicted that the net magnetization decreases from  $0.04$  to  $0.01 \mu\text{B/Fe}$  along the out-of-plane and from  $0.08$  to  $0.05 \mu\text{B/Fe}$  along the in-plane direction, which are in good agreement with the results of the magnetic measurements.

## 6. Conclusion

In summary, we have demonstrated that the multiferroic properties of BFO thin film can be effectively tuned by manipulating OOT structure of the film without changing in-plane biaxial strain state and boundary conditions. In addition, this approach allows us to avoid complex chemical modifications that have been recently proved for bulk powder forms. The tilt angle of the film was controlled by applying the differently tilt-engineered SRO platform layers, which can be simply realized by adjusting oxygen partial pressure during the growth. In consequence of the geometrically induced OOT changes and the concomitant phase transitions of the BFO films, we found a significant enhancement of the out-of-plane ferroelectric polarization for the T-BFO film (about two times larger than that of M-BFO) and a substantial increase of the in-plane net magnetization for the M-BFO film (about fivefold of that measured for T-BFO). Remarkably, it is revealed that changing the octahedral

structural coherency in bottom monoclinic/tetragonal SrRuO<sub>3</sub> platform layers can metastasize through the stoichiometric BiFeO<sub>3</sub> thin film over 25 nm—not confined as an interface phenomenon, resulting in controllable multiferroic phases. The complex interplay between octahedral tilts and polar/magnetic orders was examined by atomic-scale STEM, synchrotron X-ray scattering, and magnetic measurements, revealing that the tilt symmetry is critical to tailoring the multiferroicity. We believe that our approach opens a new pathway to practically manipulate lattice-coupled ferroic order parameters including the dramatic enhancement of ferroelectricity and magnetization in a thin film form and provides a useful research platform to understand physical connection between the OOT structure and multifunctionalities of perovskite oxides, decoupled with in-plane biaxial strain constraint.

## 7. Experimental Section

M-SRO and T-SRO films were prepared on (001)-oriented STO substrates at oxygen partial pressures of 20 and 100 mTorr, respectively, using a pulsed laser deposition technique. Sequentially, epitaxial BFO films were deposited on M-SRO or T-SRO films at 963 K. The oxygen partial pressure for the growth of BFO film was 20 mTorr. A KrF excimer laser with a wavelength of 248 nm was used, energy density of 1.5 J cm<sup>-2</sup>, and repetition rate of 2 Hz for the deposition. After deposition of BFO layers, all the films were cooled down to room temperature at a cooling rate of 20 K min<sup>-1</sup> under an oxygen partial pressure of 20 Torr. The thicknesses of BFO on M-SRO, BFO on T-SRO, M-SRO, and T-SRO films were 37.5, 37.5, 37, and 42 nm, respectively. It is to be noted that the subsequent SRO–BFO growth without selective etching yielded the formation of a RuO<sub>2</sub>–BiO layer sequence at the interface, and the etched SrTiO<sub>3</sub> substrate was predominantly TiO<sub>2</sub>-terminated, which was proved by HAADF-STEM imaging (see Figures S3c and S7c in the Supporting Information).

In order to investigate the crystallographic structures and octahedral tilt types of BFO and SRO films, X-ray scattering experiments were conducted with a high-resolution diffractometer at the 3A beamline of the Pohang Light Source with a six-circle PSI diffractometer. The photon energy was set to be 11.06 keV ( $\lambda = 1.121 \text{ \AA}$ ). The diffracted photon flux was monitored with an ion detector.

Cross-sectional thin-film samples oriented along the <110> pseudocubic direction for STEM analysis were prepared with the use of dual-beam focused ion beam (FIB, FEI Helios Nano Lab 450) slicing and lift-out processes, and the samples were additionally cleaned by low-energy Ar ion milling at 700 V (Fischione Model 1040 Nanomill) to remove any residual damaged surface layers. HAADF and ABF imaging were performed with an aberration-corrected Nion UltraSTEM200 microscope operating at 200 kV, equipped with a fifth-order aberration corrector. The convergence semiangle of the incident electron probe was about 30 mrad, and the HAADF signals for the samples were collected over a detector angle range of  $\approx 86$ –200 mrad. Random background noises in the experimental images were filtered out and the image analysis was performed with Digital Micrograph scripts. The STEM image simulation (Figure S2, Supporting Information) was carried out with a 200 kV electron probe with a probe-forming semiangle of 30 mrad and an ABF detector spanning the range of 15–30 mrad with the QSTEM<sup>[41]</sup> software package based on the multislice method.

The quality of the samples was carefully examined through the atomic-scale STEMs for several batches of samples prepared by FIB. Over 600 images were acquired as a total for the samples including EELS and EDS spectrum imaging data and found no evidence for the presence of the secondary phases inside the BFO films, thus concluding that none of any secondary structures is formed inside the BFO film or interface region within the framework of these observations (see an example shown in

Figure S13 in the Supporting Information) except for the surface region; during the FIB sample preparation, the surface parts of the samples were usually damaged.

Before the spectroscopic studies, all samples were subjected to plasma cleaning for 5 min with the mixture gas of 75% Ar and 25% O<sub>2</sub> and subsequent baking at 100 °C for 10 min to reduce carbonaceous contaminations. STEM-EDS/EELS analysis was performed on an aberration-corrected transmission electron microscope (JEOL ARM200CF) working at 200 kV equipped with EDS (JED-2300T, JEOL) and EELS (Gatan Quantum SE). Dual-type EDS detector with a large effective solid angle ( $\approx 1.2 \text{ sr.}$ ) and a highly focused electron probe ( $\approx 1.1 \text{ \AA}$ ) was used to obtain atomic resolution chemical mapping data. Each detector had the effective X-ray sensing area of a 100 nm<sup>2</sup>. The EELS collection semiangle was 44 mrad and the EEL spectra were acquired from 400 to 912 eV with the dispersion of 0.25 eV per channel and the dwell time of 0.5 s per pixel. Principal component analysis on the EEL spectrum was performed to reduce random noise. Subsequently, the background in the EEL spectrum following a power-law dependency was removed before the second derivative method to determine Fe L<sub>3</sub>/L<sub>2</sub> ratio.<sup>[42]</sup>

The ferroelectric properties of BFO films were investigated using PFM based on a commercial atomic force microscope (AFM, NX-10, Park Systems) connected with a lock-in amplifier (SR830, Stanford Research Systems).<sup>[43]</sup> An AC bias of 0.7 V<sub>rms</sub> was applied to the Pt/Cr-coated AFM probe (Multi75E-G, BudgetSensors). To measure the hysteresis loops for piezoelectric response, the AFM was connected to the LabVIEW system of a digitizer (PXI-5122, National Instruments) and waveform generator (PXI-5412, National Instruments). An AC bias of 0.5 V<sub>peak</sub> and a DC bias ranging from -4 to 4 V were applied to the conductive AFM probe with the use of a waveform generator.

Magnetic measurements were performed at 300 and 50 K with a superconducting quantum interference device magnetometer (Quantum Design MPMS XL). To eliminate noise from the silver pastes at the side and rear surface of STO substrates, the pastes were removed with the use of emery paper.

DFT calculations were employed in the local spin-density approximation (LSDA + U) scheme as implemented in the software package VASP.<sup>[44]</sup>  $U = 5 \text{ eV}$  and  $J_H = 1.5 \text{ eV}$  were used for Fe ions in the Lichtenstein scheme.<sup>[45]</sup> The projector-augmented wave method<sup>[46]</sup> was in the VASP potentials for Bi (5d, 6s, and 6p), Fe (3p, 3d, and 4s), and oxygen (2s and 2p). A  $5 \times 5 \times 5$  Monkhorst–Pack  $k$ -point grid was used for integrations within the Brillouin zone. Wave functions were described in a plane-wave basis truncated at 500 eV energy cutoff. Spin–orbit coupling was included with the bulk G-type antiferromagnetic order to determine the easy-axis and weak ferromagnetic moments by magnetic anisotropy calculation. Electric polarization was calculated with the use of the Berry phase method.<sup>[47,48]</sup> All internal atoms were relaxed within the given crystal symmetries (Cc for M-BFO, Ima2 for T-BFO) under the epitaxial strain constraint fit to SRO. Any vacuum layers were not used since the experimental films were more than 35 nm fully epitaxial-strained, so vacuum effect would be rather negligible. The calculation information in the Experimental section and the calculated structures in Figure S8 in the Supporting Information were added.

## Supporting Information

Supporting Information is available from the Wiley Online Library or from the author.

## Acknowledgements

S.S.L. and Y.-M.K. contributed equally to this work. J.Y.J. acknowledges support through grants from the National Research Foundation of Korea (NRF) funded by the Korean government (NRF-2014R1A1A3053111, NRF-2016R1D1A1A02937051, and NRF-2017K1A3A7A09016388),

- [13] U. Aschauer, R. Pfenninger, S. M. Selbach, T. Grande, N. A. Spaldin, *Phys. Rev. B* **2013**, *88*, 054111.
- [14] Z. Chen, Z. Luo, C. Huang, Y. Qi, P. Yang, L. You, C. Hu, T. Wu, J. Wang, C. Gao, T. Sritharan, L. Chen, *Adv. Funct. Mater.* **2011**, *21*, 133.
- [15] N. Balke, S. Choudhury, S. Jesse, M. Huijben, Y. H. Chu, A. P. Baddorf, L. Q. Chen, R. Ramesh, S. V. Kalinin, *Nat. Nanotechnol.* **2009**, *4*, 868.
- [16] K. Chu, B. K. Jang, J. H. Sung, Y. A. Shin, E. S. Lee, K. Song, J. H. Lee, C. S. Woo, S. J. Kim, S. Y. Choi, T. Y. Koo, Y. H. Kim, S. H. Oh, M. H. Jo, C. H. Yang, *Nat. Nanotechnol.* **2015**, *10*, 972.
- [17] J. X. Zhang, B. Xiang, Q. He, J. Seidel, R. J. Zeches, P. Yu, S. Y. Yang, C. H. Wang, Y. H. Chu, L. W. Martin, A. M. Minor, R. Ramesh, *Nat. Nanotechnol.* **2011**, *6*, 98.
- [18] F. Kubel, H. Schmid, *Acta Crystallogr. B* **1990**, *46*, 698.
- [19] Y.-M. Kim, A. Kumar, A. J. Hatt, A. N. Morozovska, A. Tselev, M. D. Biegalski, I. Ivanov, E. A. Eliseev, S. J. Pennycook, J. M. Rondinelli, S. V. Kalinin, A. Y. Borisevich, *Adv. Mater.* **2013**, *25*, 2497.
- [20] A. J. Hatt, N. A. Spaldin, C. Ederer, *Phys. Rev. B* **2010**, *81*, 054109.
- [21] C. Ederer, N. A. Spaldin, *Phys. Rev. B* **2005**, *71*, 060401(R).
- [22] J. C. Wojdel, J. Iniguez, *Phys. Rev. Lett.* **2010**, *105*, 037208.
- [23] H. Dixit, J. H. Lee, J. T. Krogel, S. Okamoto, V. R. Cooper, *Sci. Rep.* **2015**, *5*, 12969.
- [24] S. Ryu, J.-Y. Kim, Y.-H. Shin, B.-G. Park, J. Y. Son, H. M. Jang, *Chem. Mater.* **2009**, *21*, 5050.
- [25] J. Wang, J. B. Neaton, H. Zheng, V. Nagarajan, S. B. Ogale, B. Liu, D. Viehland, V. Vaithyanathan, D. G. Schlom, U. V. Waghmare, N. A. Spaldin, K. M. Rabe, M. Wuttig, R. Ramesh, *Science* **2003**, *299*, 1719.
- [26] W. Eerenstein, F. D. Morrison, J. Dho, M. G. Blamire, J. F. Scott, N. D. Mathur, *Science* **2005**, *307*, 1203.
- [27] J. Wang, A. Scholl, H. Zheng, S. B. Ogale, D. Viehland, D. G. Schlom, N. A. Spaldin, K. M. Rabe, M. Wuttig, L. Mohaddes, J. Neaton, U. Waghmare, T. Zhao, R. Ramesh, *Science* **2005**, *307*, 1203.
- [28] K. Saito, A. Ulyanenko, V. Grossmann, H. Ress, L. Bruegemann, H. Ohta, T. Kurosawa, S. Ueki, H. Funakubo, *Jpn. J. Appl. Phys.* **2006**, *45*, 7311.
- [29] A. M. Glazer, *Acta Crystallogr. A* **1975**, *31*, 756.
- [30] A. M. Glazer, *Acta Crystallogr. B* **1972**, *28*, 3384.
- [31] R. Ishikawa, E. Okunishi, H. Sawada, Y. Kondo, F. Hosokawa, E. Abe, *Nat. Mater.* **2011**, *10*, 278.
- [32] Q. He, R. Ishikawa, A. R. Lupini, L. Qiao, E. J. Moon, O. Ovchinnikov, S. J. May, M. D. Biegalski, A. Y. Borisevich, *ACS Nano* **2015**, *9*, 8412.
- [33] Y.-M. Kim, S. J. Pennycook, A. Y. Borisevich, *Ultramicroscopy* **2017**, *181*, 1.
- [34] Y.-M. Kim, J. He, M. D. Biegalski, H. Ambaye, V. Lauter, H. M. Christen, S. T. Pantelides, S. J. Pennycook, S. V. Kalinin, A. Y. Borisevich, *Nat. Mater.* **2012**, *11*, 888.
- [35] S. J. Pennycook, P. D. Nellist, *Scanning Transmission Electron Microscopy: Imaging and Analysis*, Springer Science & Business Media, Berlin, Germany **2011**.
- [36] H. J. Chang, S. V. Kalinin, A. N. Morozovska, M. Huijben, Y. H. Chu, P. Yu, R. Ramesh, E. A. Eliseev, G. S. Svechnikov, S. J. Pennycook, A. Y. Borisevich, *Adv. Mater.* **2011**, *23*, 2474.
- [37] C. T. Nelson, B. Winchester, Y. Zhang, S. J. Kim, A. Melville, C. Adamo, C. M. Folkman, S. H. Baek, C. B. Eom, D. G. Schlom, L. Q. Chen, X. Pan, *Nano Lett.* **2011**, *11*, 828.
- [38] Y.-M. Kim, A. Morozovska, E. Eliseev, M. P. Oxley, R. Mishra, S. M. Selbach, T. Grande, S. T. Pantelides, S. V. Kalinin, A. Y. Borisevich, *Nat. Mater.* **2014**, *13*, 1019.
- [39] Q. Gan, R. A. Rao, C. B. Eom, J. L. Garrett, M. Lee, *Appl. Phys. Lett.* **1998**, *72*, 978.
- [40] L. Gang, N. Ce-Wen, *J. Phys. D: Appl. Phys.* **2005**, *38*, 584.
- [41] C. T. Koch, *Determination of Core Structure Periodicity and Point Defect Density Along Dislocations* **2002**.